Materials Horizons

COMMUNICATION

ROYAL SOCIETY OF CHEMISTRY

View Article Online
View Journal | View Issue

Check for updates

Cite this: *Mater. Horiz.*, 2024, 11, 4454

Received 17th May 2024,
Accepted 20th June 2024

DOI: 10.1039/d4mh00593g

rsc.li/materials-horizons

Sulfur-regulated $CoSe_2$ nanowires with high-charge active centers for electrochemical nitrate reduction to ammonium†

Wuyong Zhang, Yingjie Wen, Haocheng Chen, Minli Wang, Caihan Zhu, Yunan Wang* and Zhiyi Lu 🆔 *

Developing high-efficiency electrocatalysts for nitrate-to-ammonia transformation holds significant promise for the production of ammonia, a crucial component in agricultural fertilizers and as a carbon-free energy carrier. In this study, we propose a viable strategy involving sulfur doping to modulate both the microstructure and electronic properties of $CoSe_2$ for nitrate reduction. This approach remarkably enhances the conversion of nitrate to ammonia by effectively regulating the adsorption capability of nitrogenous intermediates. Specifically, sulfur-doped $CoSe_2$ nanowires (S-$CoSe_2$ NWs) exhibit a peak faradaic efficiency of 93.1% at -0.6 V *vs.* RHE and achieve the highest NH_3 yield rate of 11.6 mg h^{-1} cm^{-2}. Mechanistic investigations reveal that sulfur doping facilitates the creation of highly charged active sites, which enhance the adsorption of nitrite and subsequent hydrogenation, leading to improved selectivity towards ammonia production.

New concepts

In this study, we demonstrate a new concept that regulates the nanodimensions of transition-metal dichalcogenides (TMDs) by introducing sulfur. Our sulfur doping method differs from the normal electronic regulation of materials and further modulates the morphology of the $CoSe_2$ materials from 2D to 1D by changing the supersaturation and ionization of the synthetic system. The 1D ternary S-$CoSe_2$ NWs can drive nitrate electroreduction to ammonia (NARR) with high activity and selectivity due to their advanced one-dimensional structure and high-charge active center. This is the first time that a morphology and electron-control method has been proposed to provide an advanced structure for NARR in TMDs. The significance of an advanced microstructure and electronic structure in NARR has been proven, and we are sure this is a highly innovative approach from the perspective of materials chemistry and from electrochemistry, which opens up an interesting field of research.

Introduction

Ammonia is a cornerstone of human existence, primarily fueling fertilizer production.[1–3] However, the dominant method for large-scale ammonia synthesis, the Haber–Bosch process, heavily relies on elevated temperatures and pressures, consumes nearly 2% of global energy, and contributes to approximately 1% of greenhouse gas emissions.[4–8] The electrochemical nitrogen reduction reaction (NRR) has emerged as a promising alternative, offering the potential for ammonia production under ambient conditions.[9] Nonetheless, in aqueous systems, the faradaic efficiency (FE) and partial current density typically fall below 50% and 10 mA cm^{-2}, respectively.[10–13] This significant gap between the current NRR performance and

Key Laboratory of Advanced Fuel Cells and Electrolyzers Technology of Zhejiang Province, Chinese Academy of Sciences, Ningbo, Zhejiang, 315201, P. R. China.
E-mail: luzhiyi@nimte.ac.cn, wangyunan@nimte.ac.cn
† Electronic supplementary information (ESI) available. See DOI: https://doi.org/10.1039/d4mh00593g

industrial requirements, demanding a partial current density of 300 mA cm^{-2} with 90% FE, remains a challenge.[14]

The primary obstacle to advancing NRR lies in the inertness of nitrogen (941 kJ mol^{-1} for N≡N) and its low water solubility (20 mg L^{-1}).[15] In contrast, nitrate (NO_3^-) boasts a more readily activated chemical bond (204 kJ mol^{-1} for N–O) and greater solubility, facilitating nitrate reduction reactions (NARRs) at the solid–liquid interface with a lower energy barrier.[16] Moreover, nitrate is abundant in the Earth's environment and is extensively used as a nitrogen-containing fertilizer.[17] Also, precisely because of this, its widespread use has led to pervasive nitrogen contamination, significantly impacting biodiversity.[18] Additionally, many individuals are exposed to water environments exceeding regulated nitrate limits (50 mg L^{-1}, WHO, 2004), potentially leading to health issues such as non-Hodgkin's lymphoma and methemoglobinemia.[19–21] Therefore, reversing nitrate conversion is of substantial importance for both industrial ammonia production and environmental remediation.[22]

In addition to the aforementioned merits, the NARR process generates undesirable byproducts such as dinitrogen, nitrite, and nitric oxide due to multiple electron–proton transfer processes.[23–25]

4454 | *Mater. Horiz.*, 2024, **11**, 4454–4461

This journal is © The Royal Society of Chemistry 2024

Published on 22 junho 2024. Downloaded on 06/01/2026 00:42:13.

The formation of these byproducts depends on the nitrate concentration and electrolyte pH, highlighting the need for novel materials with abundant active sites to facilitate efficient ammonia production.[26–28] While traditional efficient NARR processes often rely on noble metals like Ru-based materials, their high cost and natural scarcity pose significant barriers to widespread applications.[29–32] In contrast, transition-metal dichalcogenides (TMDs) such as $CoSe_2$ and CoS_2 have emerged as compelling candidates due to their abundance and cost-efficient production processes.[33–35] Moreover, given that electrochemical reactions predominantly occur at material surfaces or interfaces, the high specific surface area of TMDs, akin to MoS_2 for hydrogen evolution, holds promise for electrochemical energy conversion.[36–38] However, the common 2D TMDs suffer from aggregation or restacking that severely limits their potential performance, necessitating the construction of advanced structures from the molecular level to enhance the intrinsic activity of TMDs.[39,40] Furthermore, the application of TMDs in the NARR has been scarcely reported to date, highlighting the untapped potential in this domain.[41,42]

Herein, we present a novel ternary TMD, S-$CoSe_2$ nanowire, designed and synthesized for the NARR. By introducing sulfur to modulate the ionization and supersaturation of the synthetic system, the microstructure of the original binary $CoSe_2$ transitions from 2D to 1D, coinciding with the generation of high-charge cobalt centers. The resulting 1D S-$CoSe_2$ nanowire with an advanced structure exhibits pronounced nitrate-to-ammonia activity and selectivity, achieving a peak faradaic efficiency of 93.1% and the highest NH_3 yield rate of 11.6 mg h^{-1} cm^{-2}. Further theoretical studies suggest that the high-charge cobalt center enhances the adsorption of NARR intermediates, such as nitrite, for further hydrogenation.

Results and discussion

Ternary ultrathin sulfur-doped $CoSe_2$ nanowires (S-$CoSe_2$ NWs) were synthesized via a solvothermal method.[43–45] Scanning electron microscopy (SEM) images at low magnification revealed the homogeneity of the obtained materials, devoid of any other byproducts, thereby confirming the purity of the synthesized nanowires. Additionally, the SEM images indicate that the material consisted of nanowires with lengths spanning in the micrometer range, suggesting the successful fabrication of elongated nanostructures (Fig. S1, ESI†). The evolution of the porous structure of S-$CoSe_2$ NWs by the overlapping and interweaving of nanowires was corroborated by nitrogen physisorption experiments (Fig. S2, ESI†). It shows a type I(b) isotherm with a high uptake of nitrogen at high relative pressure, which indicates the adsorption of macropores according to the IUPAC classification.[46] Such a porous architecture is crucial for facilitating mass transport and increasing the active surface area, thereby enhancing the performance of electrochemical applications. Further investigation of the microstructure of S-$CoSe_2$ NWs was conducted using transmission electron microscopy (TEM). The TEM images revealed that the S-$CoSe_2$ NWs exhibited a nerve-like morphology, characterized by a flexible, smooth, and even transparent appearance (Fig. 1a). Bright-field high-resolution TEM (HRTEM) was employed to further elucidate the ultrathin nature of S-$CoSe_2$ NWs. The interplanar distance was measured to be 0.26 nm (Fig. 1b). This can be
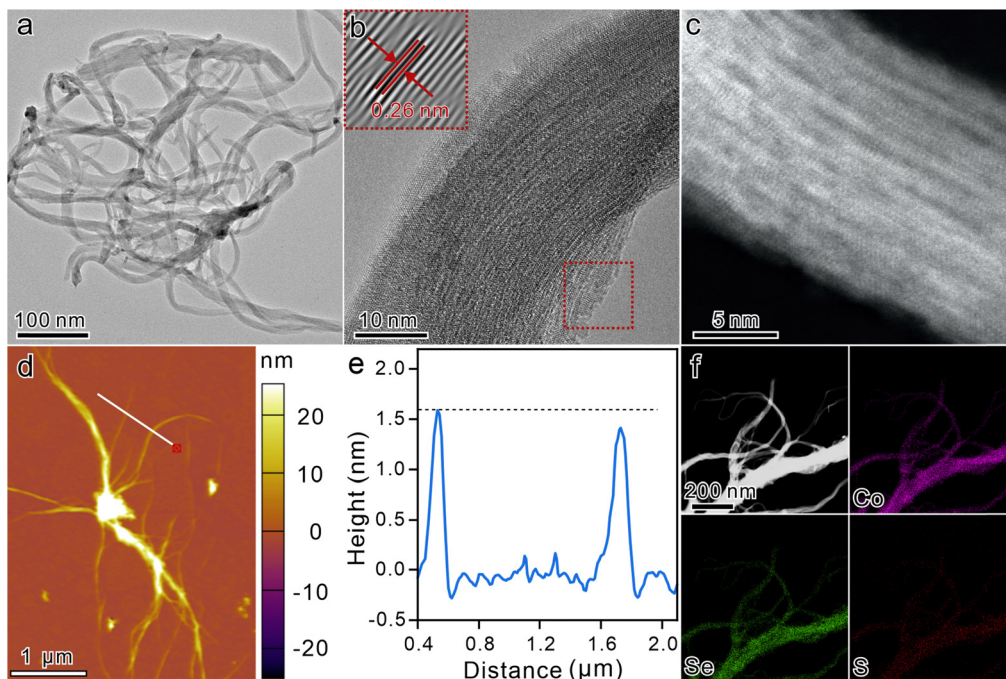

Fig. 1 Microstructure characterization of S-$CoSe_2$ NWs: (a) TEM image; (b) HRTEM image (inset image shows the lattice fringe spacing); (c) AC HAAD-STEM image; (d) and (e) AFM image and the corresponding height profile; and (f) HAAD-STEM and EDX-mapping images of all elements.

attributed to the (210) plane of the CoSe$_2$ lattice fringes, which implies that the growth direction of the S-CoSe$_2$ NWs was [210]. The polycrystalline nature of the S-CoSe$_2$ NWs was further confirmed by selected area electron diffraction (SAED) pattern analysis (Fig. S3a, ESI†), and the diffraction rings can be indexed to (210) and (311), which is in good agreement with the powder X-ray diffraction (XRD) patterns (Fig. S3b, ESI†). All observed diffraction peaks are broadening and some reflections of CoSe$_2$ are missing, which should be attributed to the ultra-thin structure of the S-CoSe$_2$ NWs.[44] Under the inspection of aberration-corrected high-angle dark-field scanning transmission electron microscopy (AC HAAD-STEM) with sub-angstrom resolution, it was clearly observed that the fasciculate nanowire had an order arrangement of atoms along the growth direction (Fig. 1c). The Raman spectrum of the S-CoSe$_2$ NWs shows an obvious peak at around 220 cm^{-1}, which can be assigned to the Se–Se stretching mode of CoSe$_2$ (Fig. S4, ESI†).[47] The thickness of S-CoSe$_2$ NWs was measured using an atomic force microscopic (AFM, Fig. 1d), and the corresponding height profile clearly shows a single S-CoSe$_2$ NWs average thickness of around 1.5 nm (Fig. 1e), which is almost equal to that of two single-unit-cell CoSe$_2$ slab.[45] SEM energy-dispersive X-ray (EDX) spectra confirm the presence of cobalt, selenium and sulfur, and the Se/Co atomic ratio was close to 2 (Fig. S5, ESI†). The corresponding EDX mapping images and line scanning clearly demonstrate the homogenous distribution of the elements (Fig. 1f and Fig. S6, ESI†). The sulfur content in S-CoSe$_2$ NWs was determined to be 4.3 at% by elemental analysis

(Table S2, ESI†). Considering this, the above results clearly demonstrate the successful fabrication of ternary S-CoSe$_2$ NWs.

The fabrication process of the S-CoSe$_2$ NWs was also further investigated. First, the formation of the S-CoSe$_2$ NWs highly relies on the reaction temperature and time. Sufficient temperature is required to generate enough solvent pressure to drive the formation of the desired morphology. By regulating the reaction temperature from 120 °C to 190 °C, it was observed that temperatures below 170 °C resulted in the formation of unexpected bulk materials, and the materials obtained individual fine nanowires at temperatures over 170 °C (Fig. S7, ESI†). With an increase of the reaction time, the material is gradually stretched to obtain a flexible and smooth nanowire morphology (Fig. S8, ESI†). Furthermore, it was found that the addition of sulfur was pivotal to forming a unique nanowire morphology. When sulfur is absent in the synthesis process, a totally different nanosheet-like material (CoSe$_2$ NSs) can be obtained (Fig. S9, ESI†). With the regulation of sulfur usage, it can be clearly observed that the material has an obvious evolutionary morphology change from nanosheets to nanowires (Fig. 2b–f and Fig. S10, ESI†). Meanwhile, the XRD patterns of CoSe$_2$ also broadened and weakened, indicating that the crystallinity of the material was poor. The slightly negative shift of the XRD peaks indicates the lattice expansion of the as-prepared materials with sulfur doping (Fig. S11, ESI†). This intriguing phenomenon drives us to elucidate the intrinsic formation mechanism of S-CoSe NWs. Ethylenediamine (EDA) was employed as the solvent and sequestrant in this system. Co^{2+}, Se, S can coordinate
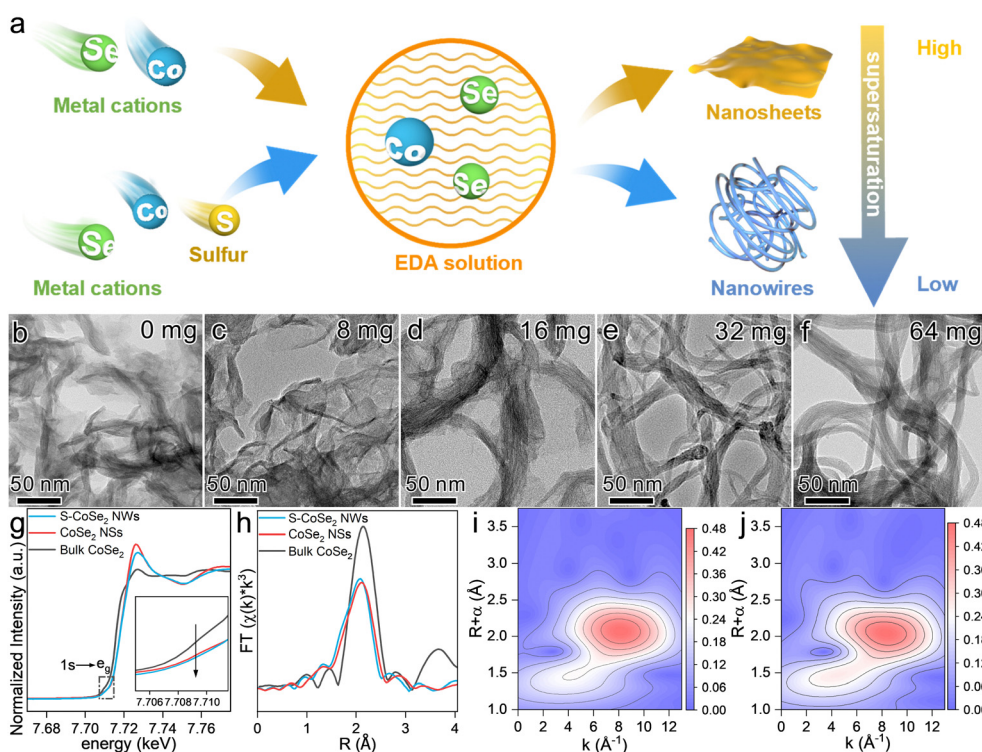

Fig. 2 (a) Formation mechanism of CoSe$_2$ NSs and S-CoSe$_2$ NWs. (b)–(f) Morphological evolution of CoSe$_2$ materials with different sulfur contents. (g) Co K-edge XANES spectra and (h) corresponding Fourier transforms of k^3-weighted EXAFS spectra for CoSe$_2$ materials. Wavelet transforms of k^3-weighted EXAFS spectra of the Co K-edge for (i) CoSe$_2$ NSs and (j) S-CoSe$_2$ NWs.

with EDA to form a series of complexes $[Co(EDA)_2]^{2+}$, $[Se_x\text{-EDA}]^-$ and $[S_x\text{-EDA}]^-$, respectively.[48] The addition of sulfur can replace the counterion for $[Co(EDA)_2]^{2+}$, which results in a blue shift in the UV-vis spectra (Fig. S12, ESI†). The distinct precursor complex also has a different supersaturation (S) of the solution and electrolytic dissociation (α) of the reactants.[49] S can influence the surface engineering of the resulting materials, and α can determine whether the growth of materials is isotropic or anisotropic.[50,51] There is no doubt that EDA is a weak electrolyte with low α ($10^{-4.07}$), which results in the anisotropic growth of $CoSe_2$ to be 2D nanosheets or a 1D nanowires, as the EDA can provide a constant and equilibrium-driven force to support the orientated growth. Moreover, the new counterion of $[S_x\text{-EDA}]^-$ in the system significantly decreases the S of the final products, which further results in a small, saturated region with a slow growth rate to obtain regularly shaped S-$CoSe_2$ NWs (Fig. 2a). Besides the morphology regulation, sulfur doping also affects the electronic states of the resulting materials. With more electronegative sulfur doping, the oxidation state of cobalt in the S-$CoSe_2$ NWs is significantly different from that of $CoSe_2$ NSs, which can be observed from the positive binding energy shift from Co 2p X-ray photoelectron spectroscopy (Fig. S13, ESI†). The local structure and coordination information of the $CoSe_2$ materials were further studied by X-ray absorption near edge structure (XANES) and extended X-ray absorption fine structure (EXAFS) spectroscopy. The main adsorption Co K-edge XANES peak shifts to higher energy after sulfur doping, which further consolidates the higher oxidation state of the S-$CoSe_2$ NWs (Fig. 2g). Moreover, $CoSe_2$ NSs and S-$CoSe_2$ NWs both show a pre-edge peak at around 7709.8 eV for the 1s to e_g intra-atomic transition in cobalt, which indicates the sulfur doping has a negligible influence on the octahedral configuration of $CoSe_2$.[52] However, it is worth mentioning that the intensity of the pre-edge peak has a perceptible decrease with sulfur incorporating, indicating the enhancive e_g filling of cobalt (inset in Fig. 2g).[52] Further extended X-ray absorption fine structure (EXAFS, Fig. 2h) spectroscopy discloses an obvious decrease of the Co–Se scattering path due to the shorter bond distance of Co–S than that of Co–Se, and the emergent Co–S scattering path in S-$CoSe_2$ NWs is clearly observed in wavelet transform analysis with the high-k direction extension (Fig. 2i and j). The corresponding EXAFS fitting also implies a monotonic decrease of the coordination number (CN) of Co–Se and increase of the CN of Co–S (Fig. S14 and Table S2, ESI†). Generally, the mechanistic investigation and spectroscopic studies on $CoSe_2$ materials reveal that sulfur doping can readily regulate not only the microstructure from 2D to 1D but also controllably tailor the electronic structure and local chemical environment of $CoSe_2$.

Based on the above analysis, $CoSe_2$ NSs and S-$CoSe_2$ NWs with distinct microstructures and electronic structures could serve as promising research platforms to explore the structure–property relationship of nitrate reduction in TMDs, and further unveil the fundamental mechanisms involved in the NARR. As doping strategy can effectively regulate the catalytic activity, and sulfur can combine with hydrogen with the p-orbital to form active hydrogen, which is considered an important

species to combine with NARR intermediates to modulate the reaction behavior.[53–57] Based on these considerations, the self-supported working electrode of the *in situ* growth S-$CoSe_2$ NWs on $1 \times 1\ cm^2$ carbon cloth (S-$CoSe_2$ NWs@CC, Fig. S15, ESI†) was employed for the NARR test, and $CoSe_2$ NSs@CC was used as a reference. The electrodes were further dwelled in an H-cell filled with 0.5 M Na_2SO_4 and 0.5 M KNO_3 as electrolytes. Linear sweep voltammetry (LSV) was initially conducted on the utilized catalysts, while both $CoSe_2$ NSs@CC and S-$CoSe_2$ NWs@CC exhibited pronounced current responses in the presence of NO_3^-. However, S-$CoSe_2$ NWs@CC had a more positive onset potential and higher current response (Fig. 3a), which can be attributed to the higher intrinsic activity and advanced porous structure with a higher BET surface area (Fig. S16, ESI†).[58] The ammonia concentration of the electrolytes for the above catalysts was investigated after chronoamperometry at -0.5 V *vs.* RHE using the indophenol blue method. Apparently, S-$CoSe_2$ NWs@CC can produce more ammonia under the same potential compared to $CoSe_2$ NSs@CC and bare CC (Fig. 3b), as indicated by the sharp peak of indophenol blue centered at 655.5 nm in the UV spectra. The NH_3 yield and the corresponding FE of the electrodes at all given potentials are further calculated from the standard curve recorded at different concentrations of NH_4^+–N (Fig. S17, ESI†). S-$CoSe_2$ NWs@CC can produce increasing amounts of ammonia with the cathodic potential boosting to be more negative, reaching the highest faradaic efficiency (FE) of 93.1% at -0.6 V *vs.* RHE and the highest rate of 11.6 mg h^{-1} cm^{-2} at -0.8 V *vs.* RHE (Fig. 3c). This can also be confirmed by the corresponding UV-vis spectra of the electrolytes after coloring (Fig. S18, ESI†). It is worth mentioning that the FE remains consistently above 90% at high potentials, indicating the remarkable selectivity exhibited by the S-$CoSe_2$ NWs. The ammonia production of the S-$CoSe_2$ NWs was additionally quantified using ^{1}H nuclear magnetic resonance (NMR) spectroscopy with maleic acid as an internal standard (Fig. S19, ESI†). An FE of 91.5% at -0.6 V *vs.* RHE was calculated, which aligns well with the results obtained from the UV-vis analysis, further corroborating the high selectivity towards ammonia (Fig. S20, ESI†). The source of nitrogen in the produced ammonia was unequivocally confirmed by ^{1}H NMR experiments employing ^{15}N isotopic labeling. As ^{15}N is a spin-$\frac{1}{2}$ nucleus that results in two symmetric signals for ^{1}H-^{15}N, in contrast to the three symmetric signals observed for ^{1}H–^{14}N interactions, which involve a spin-1 nucleus.[59] With standard ammonium salt as a reference, the electrolyte after NARR with $^{15}NO_3^-$ exhibited distinct double peaks, while triple peaks were observed with $^{14}NO_3^-$ as the nitrogen source (Fig. S21, ESI†). The NARR byproducts of S-$CoSe_2$ NWs and $CoSe_2$ NSs, nitrite (NO_2^-) and the competitive HER product of H_2 are also detected, and corresponding FEs are calculated (Fig. 3d and Fig. S22, ESI†). In the case of the S-$CoSe_2$ NWs, as the potential is progressively increased to the positive range, the FEs of nitrite gradually decrease, falling below 5%, with ammonia becoming the dominant product. Conversely, for the $CoSe_2$ NSs, a similar trend is observed with nitrite, albeit with a higher FE share. The superior selectivity towards ammonia
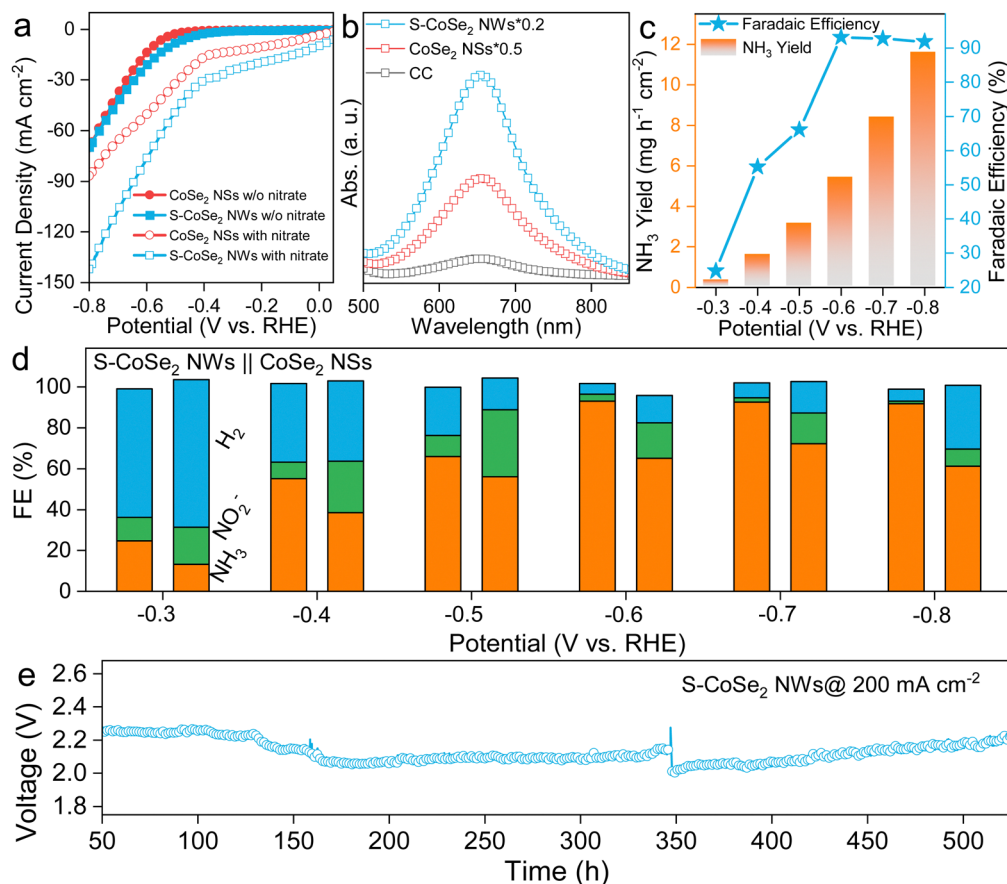
Fig. 3 (a) LSV curves of CoSe₂ NSs and S-CoSe₂ NWs in 0.5 M KOH and 0.5 M KOH + 0.5 M KNO₃, respectively. (b) UV-vis spectra of the electrolytes tested using the indophenol blue method after chronoamperometry at −0.6 V *vs.* RHE. (c) FE and NH₃ yield rates of S-CoSe₂ NWs at all potentials. (d) FE comparison between CoSe₂ NSs and S-CoSe₂ NWs at given potentials. (e) Chronopotentiometry curve of S-CoSe₂ NWs with a two-electrode system in a self-organized device (the voltage jump at 350 h is due to the replenishment of fresh electrolyte to the cell).

exhibited by the S-CoSe₂ NWs further validates the role of sulfur doping in providing higher charge active centers, which enhances the adsorption of intermediates. We further investigated the NARR performance of S-CoSe2 nanomaterials with different sulfur doping contents ranging from 0.86% to 4.3% (Fig. S23, ESI†). The FE collections clearly show an increase in the FE for the target ammonia, accompanied by a decrease in the FE for the byproduct nitrite, which strongly confirms the pivotal role of sulfur in enhancing the NARR performance. Moreover, bulk CoSe₂ was also synthesized as a reference (Fig. S24, ESI†). It exhibited inferior activity and undesirable selectivity towards ammonia, underscoring the superiority of the nanostructured S-CoSe₂ NWs (Fig. S25, ESI†). Besides activity, the stability of the S-CoSe₂ NWs is also evaluated using a long-term chronopotentiometry test in a self-organized device (Fig. S26, ESI†). We fabricated this flow cell device by coupling the S-CoSe₂ NWs@CC as the cathode and NiFe LDH@ Ni foam as the anode, which was separated by a Nafion membrane (**Fig. S27,** ESI†), under a high current of 200 mA cm⁻²; this device could continuously produce ammonia over 500 h without an obvious surge in the cell voltage. The structural integrity and electronic structure of the S-CoSe₂ NWs were further examined using TEM and XPS after a long-term reaction. The analyses revealed that

S-CoSe₂ NWs nearly retained their original microstructures and electronic configuration, underscoring their robustness (Fig. S28, ESI†). After the operation, the ammonia produced can be further fixed in the solid form of struvite ((NH₄)MgPO₄· 6H₂O) by adding a coprecipitator of Mg²⁺ and PO₄³⁻, which can be further used as fertilizer. Using this struvite-precipitation method, we obtained over 150 g of struvite with high purity (Fig. S29, ESI†). It also provides a promising way to capture nitrite and phosphate in eutrophicated water and is further convert to a value-added fertilizer.

This superior performance motivated us to investigate the reaction mechanism and uncover the reason for the distinct selectivity difference between CoSe₂ NSs and S-CoSe₂ NWs. First, *in situ* electrochemical spectroscopy was employed to identify the nitrogen-containing intermediates during NARR. Attenuated total reflection Fourier-transform infrared spectroscopy (ATR-FTIR, Fig. S30, ESI†) was performed to detect the species adsorbed on the electrode surface, and the reference spectrum obtained under open circuit potential was collected as the background. Then, the potential in the operating range was stepped from −0.3 V to −0.7 V *vs.* RHE. With increasing potential, several downward peaks emerged that were independent of the working potential, indicating the generation of

NARR intermediates. The downward bands at around 1150 cm^{-1} and 1210 cm^{-1} can be, respectively, attributed to the –N–O– stretching vibration of NH$_2$OH and the N–O antisymmetric stretching vibration of NO$_2^-$, which are both important intermediates during NARR. Furthermore, the upward band at around 1350 cm^{-1}, assigned to the asymmetric stretching vibration of NO$_3^-$, indicates the consumption of nitrate at the electrode interface.[60] For CoSe$_2$ NSs, the FTIR spectra collected were similar to those of S-CoSe$_2$ NWs, indicating the analogous NARR route on both catalysts. However, the adsorption band center of NO$_2^-$ on the CoSe$_2$ NSs has an obvious red shift to 1224 cm^{-1}, indicating the adsorption attenuation of NO$_2^-$ on the materials, which could be difficult for further hydrogenation (Fig. S31, ESI†). Besides ATR-FTIR, *in situ* electrochemical Raman spectroscopy was performed to obtain adminicular information about the intermediates during the NARR. The Raman shifts at 979 cm^{-1} and 1046 cm^{-1} can be attributed to the sulfate and nitrate groups. The peaks observed at 1373, 1535, and 1598 cm^{-1} are associated with the symmetric N–O stretches of adsorbed NO$_2^-$, N=O stretches of NOH, and H–N–H of NH$_2$, respectively.[61,62] The possible NARR intermediates were also captured by online differential electrochemical mass spectrometry (DEMS) with consecutive cycles for uncovering the integrated mechanism.[63] The major mass–charge ratio (m/z) signals of NH(15), NH$_2$(16), and NH$_2$OH (33) were definitely

captured as reaction intermediates, and NH$_3$(17) with a strong signal intensity indicates the formation of the NARR product NH$_3$. It should be noted that the m/z signal of 46 represents the possible byproduct of NO$_2^-$, and its weak intensity also reversely validates the high selectivity of S-CoSe$_2$ NWs. Combining the information provided by the above electrochemical *in situ* technologies, the nitrate reduction pathway for the given materials can be proposed as follows: NO$_3^-$ → NO$_3$* → NO$_2$* → NO* → NOH* → NOH* → N* → NH* → NH$_2$* → NH$_3$.

We further conducted density functional theory (DFT) calculations to determine the possible reaction mechanism based on the structural model of sulfur-doped CoSe$_2$ and observed the experimental evidence. First, the (210) facet was selected as the NARR surface due to its lower surface energy than that of the exposed (311) facet (Fig. S32, ESI†). As NARR is a multiple electron–proton transfer process with many intermediates and adsorption models on active sites, the most possible pathway is illustrated (Fig. 4d).[64] In terms of thermodynamics, the nitrate adsorption on sulfur-doped CoSe$_2$ is unfavorable with an uphill free energy of 0.47 eV during the entire catalytic processes, which is lower than that on CoSe$_2$ (0.55 eV, Fig. S33, ESI†). The first hydrogenation on the *NO$_3$ and *NO$_2$ (*NO$_3$ to *NO$_2$OH, *NO$_2$ to *NOOH) without electron transfer shows uphill free energies of 0.08 eV and 0.17 eV, respectively. The rate-determining step (RDS) on S-CoSe$_2$ NWs appeared on the
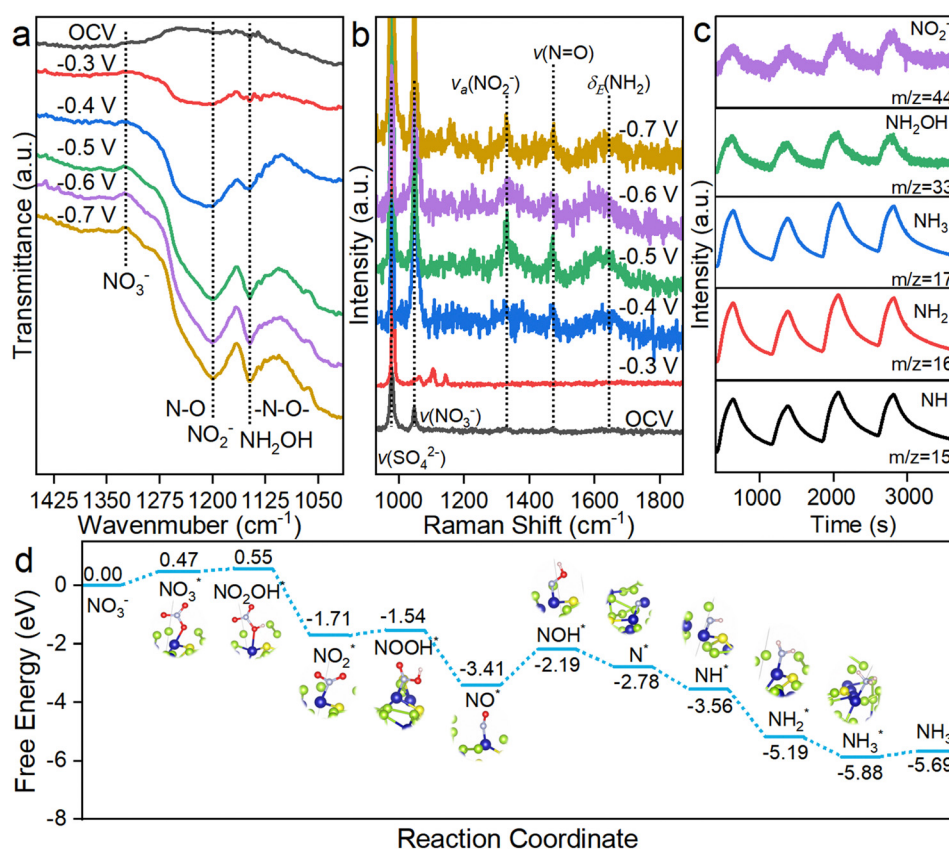

Fig. 4 (a) Electrochemical *in situ* FTIR spectra and (b) *in situ* Raman spectra of S-CoSe$_2$ NWs. (c) Online DEMS of S-CoSe$_2$ NWs under a potential of −0.35 V *vs.* RHE. (d) Reaction-free energies for different intermediates of NARR based on the model of sulfur-doped CoSe$_2$.

hydrogenation of *NO (*NO to *NOH) with a free energy increase of 1.21 eV, and $CoSe_2$ shows the same RDS but with a lower free energy increase of 1.08 eV. This result contradicts the fact that S-$CoSe_2$ NWs with lower onset potential and overpotential have higher apparent activity. This inconformity could be explained by the strong competition of H* and nitrogen-containing species produced during NARR. Sulfur has a higher *H adsorption capability, which can promote hydrogenation of NARR; however, excess *H accumulation will also lead to the decrease of NARR selectivity, and the adjacent active sites of cobalt can *in situ* utilize the produced *H to balance the kinetics of production and utilization of *H. Moreover, as mentioned before, the structural advantage of S-$CoSe_2$ NWs with a higher BET surface area and more abundant active sites cannot be ignored; it also contributes significantly towards apparent activity. The reduction steps of *NOH to NH_3* on sulfur-doped $CoSe_2$ are nearly downhill in free energy, which contributes to the remarkable catalytic performance of S-$CoSe_2$ NWs. $CoSe_2$ follows similar reaction steps and trends with sulfur-doped $CoSe_2$, but the selectivity towards NO_2^- between them is distinct at all given potentials. This could be explained by the difference in the free energy between the hydrogenation and desorption of *NO_2; this value is 0.22 eV for $CoSe_2$, which is higher than that of sulfur-doped $CoSe_2$ with a high-charge active center (0.12 eV), indicating a higher tendency of hydrogenation on the latter, which also reflects the better ammonia selectivity (Fig. S34, ESI†). The electronic structure analysis showed the higher charge state of cobalt on the S-$CoSe_2$ NWs. Combined with the above DFT calculation results, the high activity and selectivity of ammonia can be attributed to the high-charge active sites.

Conclusion

In summary, sulfur-doped $CoSe_2$ NWs were fabricated using a solvothermal method. By regulating the supersaturation and ionization degree of the synthetic system with sulfur addition, the morphology of the resulting $CoSe_2$ materials can gradually transition from 2D to 1D with the generation of a high-charge cobalt center. Owing to their structural advantages, S-$CoSe_2$ NWs contribute to their pronounced activity and selectivity in the electrochemical NARR to ammonia. A series of *in situ* electrochemical techniques combined with DFT calculations were employed to uncover the reaction pathway and mechanism. It was found that the high-charge active center of cobalt can stabilize NO_2* for further hydrogenation rather than desorption to nitrite, which increases the reaction selectivity to ammonia. This work expands the application range of TMDs for electrochemical nitrate reduction in ammonia synthesis and provides fundamental insights into the reaction mechanisms of high-charge Co active centers.

Author contributions

Wuyong Zhang: conceptualization, methodology, data curation, and writing – reviewing and editing; Yingjie Wen: data

curation; Haocheng Chen: data curation; Minli Wang: data curation; Caihan Zhu: data curation; Yunan Wang: supervision; Zhiyi Lu: funding acquisition and supervision.

Data availability

The data supporting this article have been included as part of the ESI.†

Conflicts of interest

The authors declared that they have no conflicts of interest in this work.

Acknowledgements

References

1 J. Lim, C. A. Fernández, S. W. Lee and M. C. Hatzell, *ACS Energy Lett.*, 2021, **6**, 3676–3685.

2 D. R. MacFarlane, P. V. Cherepanov, J. Choi, B. H. R. Suryanto, R. Y. Hodgetts, J. M. Bakker, F. M. F. Vallana and A. N. Simonov, *Joule*, 2020, **4**, 1186–1205.

3 H. Kobayashi, A. Hayakawa, K. D. Kunkuma, A. Somarathne and E. C. Okafor, *P. Combust. Inst.*, 2019, **37**, 109–133.

4 J. W. Erisman, M. A. Sutton, J. Galloway, Z. Klimont and W. Winiwarter, *Nat. Geosci.*, 2008, **1**, 636–639.

5 C. Smith, A. K. Hill and L. Torrente-Murciano, *Energy Environ. Sci.*, 2020, **13**, 331–344.

6 J. Humphreys, R. Lan and S. Tao, *Adv. Energy Sustainability Res.*, 2021, **2**, 2000043.

7 M. Capdevila-Cortada, *Nat. Catal.*, 2019, **2**, 1055.

8 N. Lehnert, B. W. Musselman and L. C. Seefeldt, *Chem. Soc. Rev.*, 2021, **50**, 3640–3646.

9 G. Qing, R. Ghazfar, S. T. Jackowski, F. Habibzadeh, M. M. Ashtiani, C. P. Chen, M. R. Smith, 3rd and T. W. Hamann, *Chem. Rev.*, 2020, **120**, 5437–5516.

10 S. J. Li, D. Bao, M. M. Shi, B. R. Wulan, J. M. Yan and Q. Jiang, *Adv. Mater.*, 2017, **29**, 1700001.

11 X. Yu, P. Han, Z. Wei, L. Huang, Z. Gu, S. Peng, J. Ma and G. Zheng, *Joule*, 2018, **2**, 1610–1622.

12 M. Nazemi, S. R. Panikkanvalappil and M. A. El-Sayed, *Nano Energy*, 2018, **49**, 316–323.

13 W. Zhang, S. Zhan, Q. Qin, T. Heil, X. Liu, J. Hwang, T. H. Ferber, J. P. Hofmann and M. Oschatz, *Small*, 2022, **18**, e2204116.

14 G. Soloveichik, *Renewable energy to fuels through utilization of energy dense liquids (REFUEL) Program Overview*, 2016.

15 L. Hu, Z. Xing and X. F. Feng, *ACS Energy Lett.*, 2020, **5**, 430–436.

16 Y. Xiong, Y. Wang, J. Zhou, F. Liu, F. Hao and Z. Fan, *Adv. Mater.*, 2024, **36**, 2304021.

17 F. T. Wakida and D. N. Lerner, *Water Res.*, 2005, **39**, 3–16.

18 M. Scherer-Lorenzen, C. Palmborg, A. Prinz and E. D. Schulze, *Ecology*, 2003, **84**, 1539–1552.

19 D. S. Powlson, T. M. Addiscott, N. Benjamin, K. G. Cassman, T. M. de Kok, H. van Grinsven, J. L. L'Hirondel, A. A. Avery and C. van Kessel, *J. Environ. Qual.*, 2008, **37**, 291–295.

20 J. P. van der Hoek and A. Klapwijk, *Water Res.*, 1987, **21**, 989–997.

21 M. H. Ward, S. D. Mark, K. P. Cantor, D. D. Weisenburger, V. Correa and S. H. Zahm, *Epidemiol.*, 1996, **7**, 465–471.

22 V. Rosca, M. Duca, M. T. de Groot and M. T. Koper, *Chem. Rev.*, 2009, **109**, 2209–2244.

23 H. Xu, Y. Ma, J. Chen, W.-X. Zhang and J. Yang, *Chem. Soc. Rev.*, 2022, **51**, 2710–2758.

24 J. Xu, S. Zhang, H. Liu, S. Liu, Y. Yuan, Y. Meng, M. Wang, C. Shen, Q. Peng, J. Chen, X. Wang, L. Song, K. Li and W. Chen, *Angew. Chem., Int. Ed.*, 2023, **62**, e202308044.

25 W. Zhang, S. Zhan, J. Xiao, T. Petit, C. Schlesiger, M. Mellin, J. P. Hofmann, T. Heil, R. Muller, K. Leopold and M. Oschatz, *Adv. Sci.*, 2023, **10**, e2302623.

26 J. F. E. Gootzen, P. G. J. M. Peeters, J. M. B. Dukers, L. Lefferts, W. Visscher and J. A. R. vanVeen, *J. Electroanal. Chem.*, 1997, **434**, 171–183.

27 M. Ahmadi and M. Nazemi, *Ind. Eng. Chem. Res.*, 2024, **63**, 9315–9328.

28 D. Liu, L. Qiao, S. Peng, H. Bai, C. Liu, W. F. Ip, K. H. Lo, H. Liu, K. W. Ng, S. Wang, X. Yang and H. Pan, *Adv. Funct. Mater.*, 2023, **33**, 2303480.

29 O. Peng, Q. Hu, X. Zhou, R. Zhang, Y. Du, M. Li, L. Ma, S. Xi, W. Fu, Z.-X. Xu, C. Cheng, Z. Chen and K. P. Loh, *ACS Catal.*, 2022, **12**, 15045–15055.

30 J. Li, G. Zhan, J. Yang, F. Quan, C. Mao, Y. Liu, B. Wang, F. Lei, L. Li, A. W. M. Chan, L. Xu, Y. Shi, Y. Du, W. Hao, P. K. Wong, J. Wang, S. X. Dou, L. Zhang and J. C. Yu, *J. Am. Chem. Soc.*, 2020, **142**, 7036–7046.

31 S. Han, H. Li, T. Li, F. Chen, R. Yang, Y. Yu and B. Zhang, *Nat. Catal.*, 2023, **6**, 402–414.

32 Z. Zhang, D. Y. Li, Y. C. Tu, J. Deng, H. T. Bi, Y. C. Yao, Y. Wang, T. S. Li, Y. S. Luo, S. J. Sun, D. D. Zheng, S. A. C. Carabineiro, Z. Chen, J. J. Zhu and X. P. Sun, *Susmat*, 2024, **4**, e193.

33 Q. Fu, J. Han, X. Wang, P. Xu, T. Yao, J. Zhong, W. Zhong, S. Liu, T. Gao, Z. Zhang, L. Xu and B. Song, *Adv. Mater.*, 2021, **33**, 1907818.

34 S. Manzeli, D. Ovchinnikov, D. Pasquier, O. V. Yazyev and A. Kis, *Nat. Rev. Mater.*, 2017, **2**, 17033.

35 Q. H. Wang, K. Kalantar-Zadeh, A. Kis, J. N. Coleman and M. S. Strano, *Nat. Nanotechnol.*, 2012, **7**, 699–712.

36 A. Mondal and A. Vomiero, *Adv. Funct. Mater.*, 2022, **32**, 2208994.

37 Y. Huang, Y. Sun, X. Zheng, T. Aoki, B. Pattengale, J. Huang, X. He, W. Bian, S. Younan, N. Williams, J. Hu, J. Ge, N. Pu, X. Yan, X. Pan, L. Zhang, Y. Wei and J. Gu, *Nat. Commun.*, 2019, **10**, 982.

38 B. Li, K. Nie, Y. Zhang, L. Yi, Y. Yuan, S. Chong, Z. Liu and W. Huang, *Adv. Mater.*, 2023, **35**, 2303285.

39 Y. Li, M. Wang and J. Sun, *Adv. Energy Mater.*, 2022, **12**, 2202600.

40 K. Belay Ibrahim, T. Ahmed Shifa, S. Zorzi, M. Getaye Sendeku, E. Moretti and A. Vomiero, *Prog. Mater. Sci.*, 2024, **144**, 101287.

41 M. Yu, H. Huang, J. Hu, S. Wang, J. Li and D. Wang, *J. Mater. Chem. A*, 2022, **10**, 23990–23997.

42 L. Yang and W. Zhu, *Appl. Surf. Sci.*, 2022, **596**, 153624.

43 M. R. Gao, W. T. Yao, H. B. Yao and S. H. Yu, *J. Am. Chem. Soc.*, 2009, **131**, 7486–7487.

44 Y. Liu, H. Cheng, M. Lyu, S. Fan, Q. Liu, W. Zhang, Y. Zhi, C. Wang, C. Xiao, S. Wei, B. Ye and Y. Xie, *J. Am. Chem. Soc.*, 2014, **136**, 15670–15675.

45 L. Liang, H. Cheng, F. Lei, J. Han, S. Gao, C. Wang, Y. Sun, S. Qamar, S. Wei and Y. Xie, *Angew. Chem., Int. Ed.*, 2015, **54**, 12004–12008.

46 M. Thommes, K. Kaneko, A. V. Neimark, J. P. Olivier, F. Rodriguez-Reinoso, J. Rouquerol and K. S. W. Sing, *Pure Appl. Chem.*, 2015, **87**, 1051–1069.

47 D. Kong, H. Wang, Z. Lu and Y. Cui, *J. Am. Chem. Soc.*, 2014, **136**, 4897–4900.

48 J. Lu, Y. Xie, F. Xu and L. Zhu, *J. Mater. Chem.*, 2002, **12**, 2755–2761.

49 W.-H. Lai, Y.-X. Wang, Y. Wang, M. Wu, J.-Z. Wang, H.-K. Liu, S.-L. Chou, J. Chen and S.-X. Dou, *Nat. Chem.*, 2019, **11**, 695–701.

50 X. Zhang and Y. Xie, *Chem. Soc. Rev.*, 2013, **42**, 8187–8199.

51 H. X. Lin, Z. C. Lei, Z. Y. Jiang, C. P. Hou, D. Y. Liu, M. M. Xu, Z. Q. Tian and Z. X. Xie, *J. Am. Chem. Soc.*, 2013, **135**, 9311–9314.

52 M. Sano, *Inorg. Chem.*, 1988, **27**, 4249–4253.

53 F. Lei, W. Xu, J. Yu, K. Li, J. Xie, P. Hao, G. Cui and B. Tang, *Chem. Eng. J.*, 2021, **426**, 131317.

54 X. Chen, Z. Qiu, H. Xing, S. Fei, J. Li, L. Ma, Y. Li and D. Liu, *Appl. Catal., B*, 2022, **305**, 121030.

55 K. Wang, R. Mao, R. Liu, J. Zhang and X. Zhao, *Appl. Catal., B*, 2022, **319**, 121862.

56 N. Xue, Z. Lin, P. Li, P. Diao and Q. Zhang, *ACS Appl. Mater. Interfaces*, 2020, **12**, 28288–28297.

57 Z. Li, L. G. Yu, C. X. Bi, X. Y. Li, J. Ma, X. Chen, X. Q. Zhang, A. B. Chen, H. T. Chen, Z. R. Zhang, L. Z. Fan, B. Q. Li, C. Tang and Q. Zhang, *Susmat*, 2024, **4**, e191.

58 Y. Li, Z. Kan, L. Jia, D. Zhang, Y. Hong, J. Liu, H. Huang, S. Li and S. Liu, *Trans. Tianjin Univ.*, 2023, **29**, 313–320.

59 D. Cremer and J. Grafenstein, *Phys. Chem. Chem. Phys.*, 2007, **9**, 2791–27816.

60 J.-Y. Fang, Q.-Z. Zheng, Y.-Y. Lou, K.-M. Zhao, S.-N. Hu, G. Li, O. Akdim, X.-Y. Huang and S.-G. Sun, *Nat. Commun.*, 2022, **13**, 7899.

61 S.-E. Bae, K. L. Stewart and A. A. Gewirth, *J. Am. Chem. Soc.*, 2007, **129**, 10171–10180.

62 D. P. Butcher and A. A. Gewirth, *Nano Energy*, 2016, **29**, 457–465.

63 Y. Yao, S. Zhu, H. Wang, H. Li and M. Shao, *Angew. Chem., Int. Ed.*, 2020, **59**, 10479–10483.

64 Y. C. Zeng, C. Priest, G. F. Wang and G. Wu, *Small Methods*, 2020, **4**, 2000672.